Pulsed Fiber Lasers with Multimode Interference Saturable Absorber

Arslan Anjum

McGill

Department of Electrical and Computer Engineering
McGill University
Montréal, Canada

December 2021

A thesis submitted to McGill University in partial fulfillment of the

requirements of the degree of Master of Science.

Abstract

Modelocked mid-infrared (mid-IR) lasers are an essential tool for applications like spectroscopy, metrology and laser surgery. They provide narrow pulse width and high peak power, which also makes them an ideal source for parametric oscillators and supercontinuum generation. Development of fiber based mid-IR ultrafast lasers is limited by the availability of fiber components like optical isolators, couplers and saturable absorbers that are compatible with operation in the wavelength window of 2-12 µm.

This thesis investigates the design of a fiber based saturable absorber that is suitable for modelocking mid-IR fiber lasers. The saturable absorber is based on nonlinear multimode interference in a multimode fiber and it operates in reflection mode. The all-fiber design of the saturable absorber eliminates the need for free-space alignment. Furthermore, the reflection mode operation makes it suitable for linear cavity laser design, which removes the need for optical isolators and additional fiber couplers. First, the proposed saturable absorber is constructed with a silica based graded index multimode fiber. This saturable absorber leads to generation of modelocked noise-like pulses in a thulium doped fiber laser. Afterwards, a mid-IR compatible version of the saturable absorber is built using an As-S-Se based step index multimode fiber. Using this device, stable mode-locked operation and resembling pulse operation are demonstrated at a wavelength of 1.9 µm.

Résumé

Les lasers infrarouge moyen (mid-IR) à verrouillage de mode sont un outil essentiel pour des applications telles que la spectroscopie, la métrologie et la chirurgie laser. Ils fournissent une largeur d'impulsion étroite et une puissance de crête élevée, ce qui en fait également une source idéale pour les oscillateurs paramétriques et la génération de supercontinuum. Le développement de lasers mid-IR ultrarapides à fibre est limité par la disponibilité de composants à fibre tels que des isolateurs optiques, des coupleurs et des absorbants saturables qui sont compatibles avec un fonctionnement dans une plage de longueur d'onde de 2 à 12 μm.

Cette thèse étudie la conception d'un absorbant saturable à fibre, utile pour verrouillage de mode des lasers mid-IR à fibre. L'absorbant saturable est basé sur une interférence multimode non linéaire dans une fibre multimode et il fonctionne en mode réflexion. La conception entièrement en fibres de l'absorbant saturable élimine le besoin d'alignement en espace libre. De plus, le fonctionnement en mode réflexion le rend adapté à la conception de lasers à cavité linéaire, ce qui élimine le besoin d'isolateurs optiques et de coupleurs de fibres supplémentaires. Premièrement, l'absorbant saturable proposé est construit avec une fibre multimode à gradient d'indice à base de silice. Cet absorbant saturable conduit à la génération d'impulsions de type bruit à verrouillage de mode dans un laser à fibre dopée au thulium. Ensuite, une version compatible mid-IR de l'absorbant saturable est construite à l'aide d'une fibre multimode à saut d'indice basée sur As-S-Se. À l'aide de cet appareil, un fonctionnement en mode verrouillé stable et un fonctionnement en impulsion ressemblant sont démontrés à une longueur d'onde de 1.9 μm.

Acknowledgments

I would like to thank my supervisor Prof. Martin Rochette for his generous support and guidance during my stay at McGill University. His meticulous work ethic and passion for nonlinear optics has always inspired me to improve my work.

Secondly, I want to express gratitude to my spouse Hiba Riaz who helped me every step of the way during this time. I also want to thank my mother and my siblings for their prayers and encouragement to pursue graduate studies.

Lastly, I would like to thank all members of the Nonlinear Photonics Group at McGill for their help. I appreciate the guidance and encouragement received over the years from Mohsen Rezaei. Special thanks to Yanjia Lyu and Kaixaun Zhang who helped me in getting started with the experimental work.

Contents

List of Figures

Chapter 1

Introduction

Ultrafast mid-infrared laser sources in the wavelength range of 2μm–5μm have generated substantial research interest in recent years due to their numerous applications in spectroscopy, bio-medicine and material processing. This wavelength region contains vibrational absorptions of several molecules like H_2O, CO and NO, hence mid-infrared ultrafast laser based spectroscopy is a vital tool for detection and measurement of such molecular species [1]. Conventionally, optical parametric oscillators (OPOs) have been used to provide high power and short width pulses for mid-infrared applications. OPOs require cumbersome alignment of free-space components [2]. Fiber based lasers provide a more compact, robust and economical alternate for generation of ultrafast pulses in the mid-infrared.

Development of fiber based ultrafast mid-infrared sources has been limited by the availability of mid-infrared compatible components like optical couplers, gain media and saturable absorbers. Passive saturable absorbers are vital for triggering pulsed regime in ultrafast lasers. They provide an intensity dependent transmission / reflection that leads to preferential attenuation of low intensity light and amplification of high intensity light. The goal of this research is to find

a fiber based saturable absorber (SA) with design flexibility and mid-infrared compatibility. Such a SA can be used to create Q-switched and modelocked laser sources at various wavelengths of interest in mid-infrared e.g. 2 μm, 2.8 μm and 3.4 μm.

Silica fibers have seen tremendous amount of research and development due to their application in telecommunication industry. These fibers provide low loss transmission around 1550 nm wavelength. Furthermore, silica is a good host for rear-earth metal dopants that can be used create active components amplifiers and lasers. The range of operation for these silica-based fiber components has been limited to wavelengths below 2.2 μm due absorption of mid-infrared light in silica. Consequently, development of fiber lasers and other components in mid-infrared has lagged behind their silica counterparts in 1−2 μm wavelength range.

Chalcogenide glass (ChG) fibers and fluoride fibers such as ZBLAN (ZrF_4-BaF_2-LaF_3-AlF_3-NaF) have emerged as promising alternatives to silica based fibers for the mid-infrared [3,4]. Both of these glass families are transparent in the mid-infrared, however they possess different properties that make them suitable for different type of applications. ChG based fibers have a high coefficient of nonlinearity compared to silica and ZBLAN fiber so they are an excellent candidate for designing nonlinear applications of mid-infrared light. ZBLAN fibers on the other hand, show good solubility for rare-earth metal ions compared to ChG fibers, hence they are more suitable for making active devices like lasers and amplifiers in the mid-infrared.

Using a step index silica multimode fiber (MMF), an MMI-SA has been demonstrated to produce modelocked pulses at a wavelength of 1.6 μm, with a pulse-width of ~0.625 ps [5]. However, silica fibers exhibit high transmission loss beyond 2 μm. On the other hand,

chalcogenide glass (ChG) fibers like As_2Se_3 and As_2S_3 exhibit excellent transparency in the mid-infrared region. Figure 1.1 shows the transmission spectrum of sulfide, selenide, and telluride chalcogenide glasses. Building an MMI-SA with ChG step index fiber can allow for modelocking operation at longer wavelengths than 2 μm. Furthermore, such a fiber-based design can be employed to realize all-fiber modelocked lasers in the mid-infrared region that are more robust, compact and durable than their free-space counter parts.
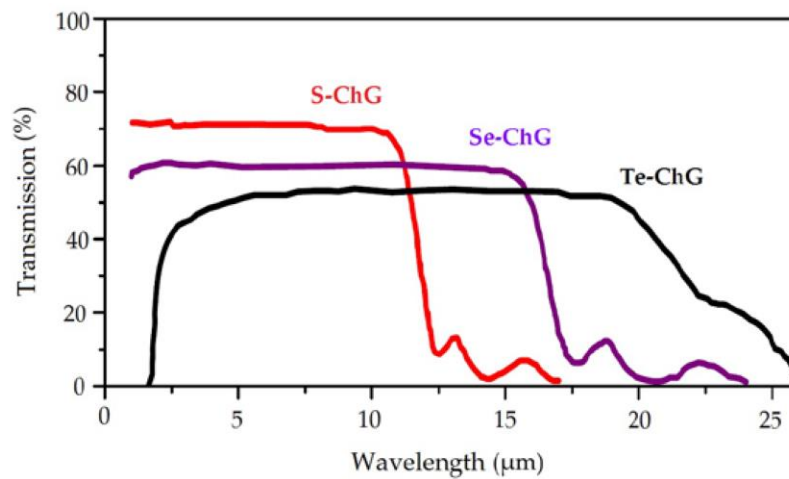
Figure 1.1 Mid-infrared transmission in bulk Selenide (Se-) Sulfide (S-) and Telluride (Te-) based chalcogenide glasses (ChG) [6]

1.1. Literature Review

A multimode interference saturable absorber (MMI-SA) relies on nonlinear interaction of various modes of a multimode fiber to provide intensity dependent loss in laser cavity. The idea of an MMI-SA based of graded index multimode fiber (GIMF) that was sandwiched between single mode fibers (SMF) was proposed in 2013 by Mafi et. al. [7]. They derived the analytical expression for saturable absorption in a SMF-GIMF-SMF structure and calculated saturation parameters like modulation depth and saturation intensity based on the modes excited in the GIMF. However, it was challenging to excite higher order modes in a GIMF spliced with SMF. Furthermore, the length of GIMF had to be controlled precisely which was difficult to implement in practice. The first demonstration of modelock laser with an MMI-SA was reported in 2017 [8]. In this work an intermediate step index multimode fiber (SIMF) was used between the SMF and GIMF to facilitate excitation of higher order modes. In a thulium (Tm)-doped fiber laser cavity, this SMF-SIMF-GIMF-SMF structure produced ultrafast pulses at 1888 nm wavelength with a pulse width of 1.2 ps. Soon afterwards, similar hybrid SIMF-GIMF structures were used in erbium (Er)- and ytterbium (Yt)- doped laser cavities to produce modelocked pulses at 1560 nm [9] and 1030 nm [10] respectively. Since then, MMI-SA based modelocked lasers have been a hot topic for research. Several other mechanisms have been tested for improving coupling into higher order GIMF modes like stretching, bending, off-set coupling and using no-core fiber mode adapters. Furthermore, MMI-SA have been employed to generate different kind of modelocked pulses besides the conventional solitons e.g. noise like pulses [11], stretched solitons [12], resembling pulses [13] and higher harmonic pulses [14]. MMF fibers other than silica based GIMF have also

been tested. Particularly, SAs with silica based [5] and chalcogenide based step index multimode fiber [13] have been demonstrated.

These reports employ a transmission mode saturable absorber in a ring cavity configuration. However, a linear cavity configuration might be more attractive for certain applications like fiber lasers beyond 2 µm wavelength as it can operate without the need of an optical isolator. This work investigates a silica GIMF SA and a chalcogenide SIMF SA in reflection mode that are compatible for linear laser cavities.

The nonlinear photonics group at McGill University focuses on the fabrication of all-fiber components such as chalcogenide tapers [15–19], optical fiber couplers [19–21], optical filters [22–25], and microsphere resonators [26–28], optical fiber devices such as spectroscopy instruments [29], frequency resolved optical gating devices [30,31], and optical fiber sources such as wavelength converters [32–41], supercontinuum sources [42–46], high-power fiber lasers [47], frequency combs [48–50], fiber lasers based on nonlinear Raman and parametric gain [51–62], bi-directional fiber lasers [63], Mamyshev oscillators [64–71], and microwave signal sources [72–74]. The saturable absorber in reflection mode presented in this thesis is a key component for the fabrication of an all-fiber mode locked laser at a wavelength of 2.8 µm. This source is envisioned to play a central role for the nonlinear photonics group as it will serve as a pump laser for mid-infrared fiber lasers, wavelength converters, fiber-optic parametric oscillators, and supercontinuum generation sources.

1.2. Thesis Outline

The thesis evaluates the performance to two MMI-SAs in reflection mode. In chapter 2, the theoretical framework needed to understand the work is presented. In chapter 3, a graded index silica multimode fiber based MMI-SA is presented. The construction process and characterization of the SA are reported. The SA is placed in linear fiber laser cavity to produce modelocked noise like pulses at a wavelength of 1.9 μm. In chapter 4, an As-S-Se step index multimode fiber based saturable absorber is presented. Such a device can operate beyond 2 μm wavelength, hence it provides critical groundwork for construction of modelocked fiber lasers in the mid-infrared. Finally, a brief summary of the work is presented along with suggestions for future research work on this topic.

Chapter 2

Basic Concepts

Modelocked lasers (MLL) are complex systems that can generate pulses with high energy and peak power. In this chapter, the underlaying physics of a MLL is discussed and formation of modelocked pulses by insertion of a saturable absorber in CW laser cavity is presented. Furthermore, an overview of the saturable absorption mechanism in multimode fiber is provided. This chapter summarizes the theoretical framework required to understand the work presented in the rest of the thesis.

2.1. Mode Locked Lasers

Initial demonstrations of laser sources produced coherent light with constant output power. Such sources, called CW (continuous wave) lasers, provided higher intensity than what was available through broadband incoherent light sources. In the early 1990's, commercialization of solid-state pulsed lasers [75] enabled a plethora of new applications by providing short bursts of coherent light with higher peak intensity. Over the years, research have been carried out in achieving higher peak intensity, shorter pulse duration and expanding pulsed operation to new wavelengths. Each

of these research themes has unique underlaying changes and they promise to unlock a different set of applications. A brief introduction of the underlaying physics in a modelocked laser is given here.

A CW lasers cavity consists of a gain medium and an oscillator that couples out some of the energy. Figure 2.1 shows a simple linear cavity, with a gain medium, a fully reflecting and a partially reflecting mirror. The oscillator comprising the two mirrors forms stationary waves at certain wavelengths, called the modes of the oscillator. The modes are separated in wavelength/frequency by a regular interval called the free spectral range (FSR). For a linear cavity the FSR is given by the following expressions.

$$f_{FSR} = \frac{c}{2\,n_g L} \qquad\qquad \lambda_{FSR} = \frac{\lambda^2}{2\,n_g L} \qquad\qquad \text{Eq. 2.1}$$

Here f_{FSR} and λ_{FSR} represents the free spectral range in frequency and wavelength. Whereas, λ is the central wavelength, n_g is group refractive index of the medium and 2L represents the roundtrip cavity length. When pumping mechanism for the gain medium is switched on, it produces light over a broad wavelength range due to spontaneous emission. The gain medium also amplifies any light reflected from the mirrors. Figure 2.2 shows the various modes of the laser along with gain bandwidth. In equilibrium, one or more neighboring modes dominate the laser output due to gain saturation. Since the mutual phase of the modes in not fixed, output intensity is constant.
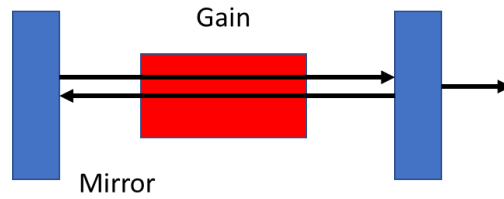
Figure 2.1. A simple laser cavity
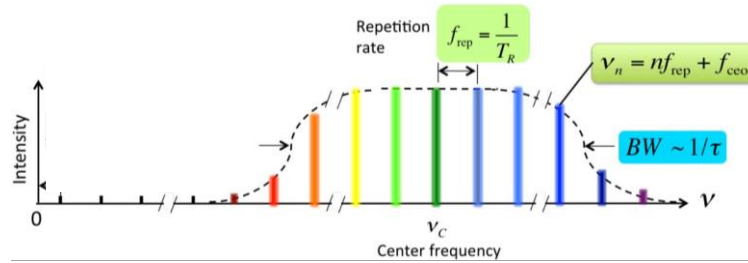
Figure 2.2. Modes of laser cavity and gain bandwidth (BW) of the medium [76]

Assume that there are (2M+1) modes in the laser output. The modes can be represented as

$$E(t) = \sum_{n=-M}^{M} E_n \exp(i\phi_n - i\omega_n t) \qquad \text{Eq. 2.2}$$

Here E_n, f_n and w_n are the amplitude, phase and frequency of nth mode respectively. If their mutual phase is random, the total intensity I(t) is constant.

$$I(t) = \sum_{n=-M}^{M} |E_n|^2 = const \qquad \text{Eq. 2.3}$$

If the mutual phase is fixed such that any two adjacent modes have a constant phase difference ϕ, it leads to formation of pulsed output in the time domain [77]. Such a fixed phase difference can be provided by modulating the light of cavity modes at a frequency of f_{FSR}. In the frequency domain, the side lobes generated due to amplitude modulation couple adjacent modes and result

in fixing/locking of the mutual phase. This modulation can be provided by an active modulator or a passive saturable absorber. If we assume that all of modes have equal amplitude E_0, the expression for intensity can be simplified as below.

$$I(t) = \frac{\sin^2([2M+1]\pi f_{FSR}t + \phi/2)}{\sin^2(\pi f_{FSR}t + \phi/2)} E_0^2 \qquad \text{Eq. 2.4}$$

Figure 2.3 shows a plot of intensity expression for M = 2 and M = 3, with f_{FSR} = 10 MHz. It is evident that the pulse duration decreases as the bandwidth of the locked modes is increased. Since the modes are separated in frequency by f_{FSR}, the bandwidth of locked modes is (2M+1) f_{FSR}. The pulse width can be estimated by t_p = 1/(2M+1) f_{FSR} as described in Ref. [77]. However, in a practical laser, the optical nonlinearity and dispersion of the cavity elements also effect the final pulse width. The nonlinearity results in broadening of the optical spectrum of the pulse while dispersion alters the pulse width in time domain. The pulses are separated by a period of t_r = 1/f_{FSR}, which is called the round-trip cavity time. The interference pattern of phase locked modes is equivalent to a single pulse circulating in the cavity at round trip time t_r.
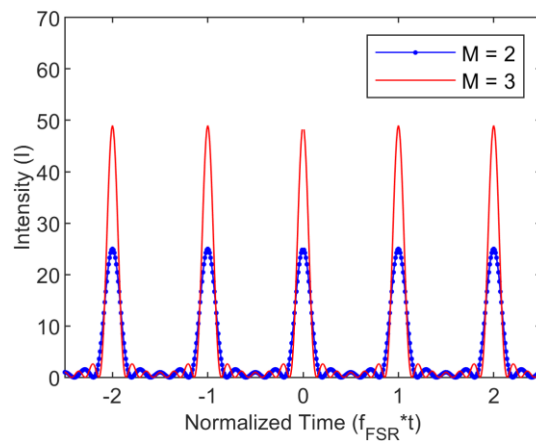
Figure 2.3. Intensity pattern for different number of locked modes

A passive saturable absorber is an optical element that provides intensity dependent transmission/reflection. Figure 2.4 shows a schematic of the laser cavity with a saturable absorber. The saturable absorber provides loss modulation at cavity repetition rate ($f_r = 1/t_r = f_{FSR}$) and results in of locking/fixing of the mode phases. Such a laser producing pulsed output is called a modelocked laser.
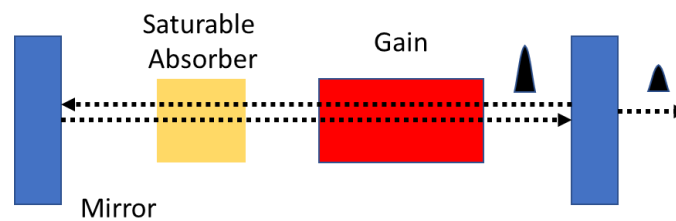
Figure 2.4. Modelocked laser with a passive saturable absorber

2.2. MMI Saturable Absorber

The multimode interference based saturable absorber (MMI-SA) can provide an all-fiber mechanism for modelocking of fiber lasers. First MMI-SA was proposed in [7]. Figure 2.5 shows a typical transmission mode MMI-SA that consists of multimode fiber (MMF) that is sandwiched between an input and output single mode fibers (SMF).
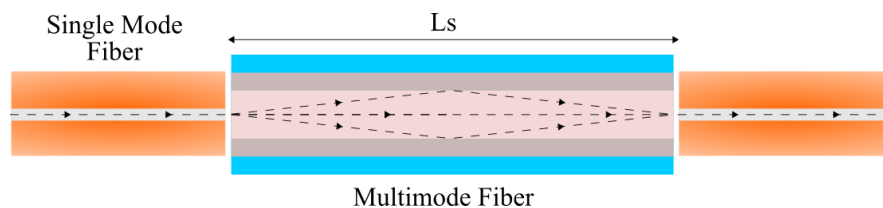
Figure 2.5. Multimode interference saturable absorber. Ls: self-imaging length.

At the input end of MMF, light from the fundamental mode of SMF can be expressed as a superposition of the various excited modes in the MMF, in terms of the electric field

$$E_{SMF}(r,\phi,z=0) = \sum_{n=1}^{N} C_n E_n(r,\phi,z=0) \qquad \text{Eq. 2.5}$$

Here, E_{SMF} is the fundamental mode of the SMF, E_n is the nth mode in the MMF and C_n is the mode expansion coefficient that can be calculated for each mode through mode overlap integrals [5]. After traveling a distance z in the MMF, each mode acquires a phase depending on its propagation constant β_n. The electric field at the output end of the MMF is then written as

$$E_{MMF}(r,\phi,z) = \sum_{n=1}^{N} C_n E_n\, e^{-i\beta_n z} = e^{-i\beta_1 z} \sum_{n=1}^{N} C_n E_n e^{-i(\beta_n - \beta_1)z} \qquad \text{Eq. 2.6}$$

While the common phase factor $e^{-i\beta_1 z}$ can be dropped, the $e^{-i(\beta_n - \beta_1)z}$ factor vanishes at some periodic distance L_s such that all the excited modes satisfy

$$\beta_1 L_s + q\, 2\pi = \beta_n L_s \qquad \text{Eq. 2.7}$$

L_s is called the self imaging length of the MMF. In a nonlinear medium, each mode acquires additional phase as it experiences self-phase modulation (SPM) and cross-phase modulation (XPM). The complex amplitude A_n of each mode at a distance z can be given by Eq. 2.8 which is derived in Ref. [5].

$$A_n(z) = A_n(0)\, e^{i\gamma_n P_n z} \qquad \text{Eq. 2.8}$$

Here γ_n is nonlinearity constant. P_n is defined as ($|A_n|^2 + 2 \sum_{m \neq n} \rho\, |A_m|^2$) to incorporate the effect of SPM and XPM. Whereas, ρ is the mode overlap factor between modes m and n. With the additional $e^{i\,(\gamma_n P_n)\, z}$ phase factor, the modified imaging length L_s' is given by

$$\beta_1 L'_s + q\, 2\pi + \gamma_1 P_1 L'_s = \beta_n L'_s + \gamma_n P_n L'_s$$

$$L'_s = \frac{\beta_1 - \beta_n}{(\beta_1 - \beta_n) + (\gamma_1 P_1 - \gamma_n P_n)} L_s$$

Eq. 2.9

Which can be rewritten as

$$L'_s = \frac{L_s}{1 + P_1 (\gamma_1 - \gamma_n C_1)\, C_2}$$

Eq. 2.10

Here $C_1 = P_n/P_1$ and $C_2 = 1/(\beta_1 - \beta_n)$ remain constant if lateral alignment of the MMF and SMFs is fixed. At low input power, when the nonlinear effects are negligible, maximum power is transmitted through the output SMF when the length of the MMF is mL_s, where m is an integer. In this case, an exact image of input SMF mode profile is regenerated at the output SMF, which has the maximum output coupling efficiency. Furthermore, Eq. 2.10 shows that imaging length decreases due to fiber nonlinearity as the incident power is increased. Let's consider a case where the length of the MMF is chosen to be slightly smaller than mL_s. At low input power, the output transmission is low due the imaging length mismatch. As the input power is increased, $P_1 \propto |A_1|^2$ also increases and the modified imaging length, $L_s{}'$ becomes smaller than L_s as predicted by Eq. 2.10. When P_1 is increased further, selected length of the MMF becomes equal to $mL_s{}'$ and the maximum power transmission is achieved. Hence such a device can provide high transmission loss at low incident power and low transmission loss at high incident power i.e. saturable absorption.

Figure 2.6 shows the power dependent transmission for such a device, which is equivalent to the saturable absorption curve of a typical semiconductor saturable absorber mirror (SESAM). One can also convert the transmission mode MMI-SA into a reflection mode device by replacing

the output fiber with a mirror or a reflective coating. This design configuration is investigated further in chapters 3 and 4.

$$T(I) = 1 - M \times e^{-\left(\frac{I}{I_{sat}}\right)} - A_{ns}$$
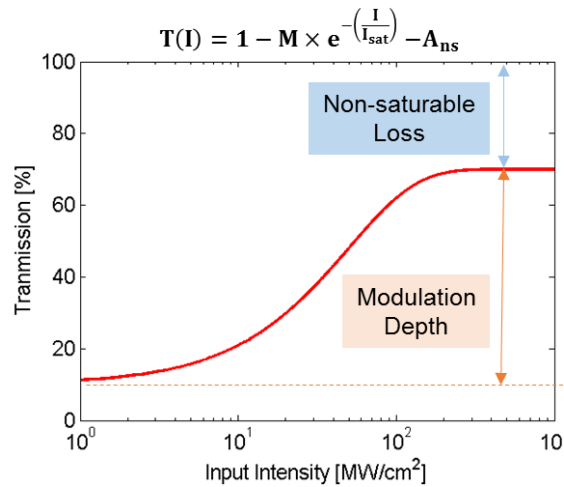
Figure 2.6. Typical transmission of an MMI saturable absorber. I: input intensity,

M: modulation depth, I_{sat}: saturation intensity, A_{ns}: Non-saturable loss

Once the MMI-SA structure is placed in fiber laser cavity, the intensity dependent transmission/reflection leads to generation of pulsed output thorough modelocking. The pulse duration and energy depend on parameters of the cavity like total dispersion and gain coefficient, as well as the parameters of the SA like modulation depth, saturation intensity and non-saturable loss. The impact of cavity and SA parameters on pulse formation is an area of active research and its details are beyond the scope of this thesis. In general, a SA with low non-saturable loss and low saturation intensity is desirable to achieve modelocking at low pump power.

Chapter 3

Silica MMI Saturable Absorber

Silica-based optical fibers have been successfully commercialized due to the intense research and development efforts in high-speed optical communication. Several single mode and multimode fibers of various diameters are readily available in the market. Compared to chalcogenide- and fluoride- based soft glass fibers, silica-based fibers are also more shock resistant and easier to process. Despite being limited to operation under 2 μm wavelength, they provide a robust testing ground for development of fiber laser sources.

In this chapter, a silica-based graded index multimode fiber (GIMF) is used to construct a multimode interference (MMI) saturable absorber (SA) in reflection mode. The all-fiber device consists of a GIMF sandwiched in between a single mode fiber and a mirror. The MMI-SA is characterized in the wavelength band of 2000 nm. It has a modulation depth of 12% and saturation intensity of 18.5 MW/cm^2. The operation of the MMI-SA is validated by triggering pulses in a thulium doped fiber laser (TDFL) in linear configuration, leading to mode locking with noise like pulses (NLP) with narrow pulse width of 365 fs and a broad optical bandwidth of 11.2 nm.

3.1. MMI Saturable Absorber in Reflection

Figure 3.1 shows a schematic of the proposed MMI-SA. It consists of silica-based GIMF from Corning Inc. that has core diameter 62.5 μm and an arbitrary length of 13 cm. A single mode fiber (SMF) is spliced to one end of the GIMF using UV-epoxy. The SMF serves as the input and output of the SA. Silica-based GIMF and SMF are used for the current experiment, but chalcogenide- or fluoride-based fibers could be used to preserve compatibility of the MMI-SA with the mid-infrared. A silver coated mirror is placed at the other end of the GIMF to reflect light back to the GIMF and SMF.
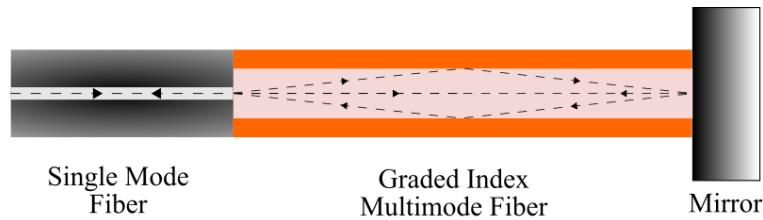
Figure 3.1. Nonlinear multimode interference saturable absorber.

Light form the SMF is coupled into various modes of the MMF depending on the lateral alignment between SMF and MMF. These modes travel through the MMF and back while accumulating different phase. The power coupled back from the MMF to the SMF is a function of the modal interference pattern at the MMF facet. This interference pattern is a function the input signal power that makes a perturbation on the phase acquired by the modes in the MMF due to self-phase modulation and cross-phase modulation [5]. The lateral offset between SMF and MMF is fixed such that it provides constructive interreference for high power input signal, leading to a power dependent reflection coefficient. Hence the structure acts as an artificial saturable absorber.

Figure 3.2 shows the setup used to measure the nonlinear reflection coefficient of the MMI-SA. Pulses from a modelocked laser (MLL) with a central wavelength of 1937 nm and width of 800 fs are sent to the MMI-SA through a circulator. A variable optical attenuator (VOA) is used vary the input power to the MMI-SA. The incident peak power reaching the SA can be varied from 0 to 112 W. After the VOA, pulses from the MLL travel 3 m in SMF before reaching the SA and acquire a nonlinear phase-shift up to 0.34 rad, an amount too low to distort the pulse spectrum significantly. The incident and reflected power of the SA is recorded using calibrated power meters PM1 and PM2 respectively.
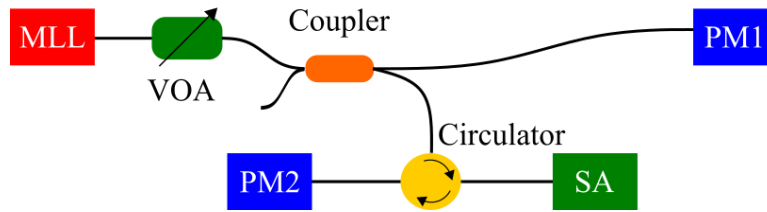
Figure 3.2. Characterization setup for MMI-SA. MLL: Mode-locked laser, VOA: Variable optical attenuator, PM: Power meter.

Figure 3.3 shows the reflection coefficient of the MMI-SA as a function of incident power. At low incident power, the MMI-SA provides a reflection coefficient of 31%. As the incident power is increased, the reflection increases up to 42.2%. The theoretical reflection coefficient profile is given by

$$R = 1 - M \exp\left(-\frac{I}{I_{sat}}\right) - A_{ns} \qquad \text{Eq. 3.1}$$

Here I represents the incident intensity, M is the modulation depth, A_{ns} is non-saturable loss and I_{sat} is the saturation intensity. A least-squares fit enables extraction of these parameters from the

measurement results. The experimental data fits this function perfectly with the use of $M = 12\%$, $A_{ns} = 57\%$ and $I_{sat} = 18.5$ MW/cm^2. In the current setup, the incident peak power in the SMF that is required to reach an optical intensity I_{sat} is 32.7 W.

Figure 3.3. Nonlinear reflectance of MMI-SA as a function of incident intensity.

3.2. Modelocked Laser

Figure 3.4 shows a schematic of the proposed laser cavity, including the MMI-SA. The gain is provided by a 23 cm long thulium-doped fiber (TDF) with a core diameter of 6 μm and numerical aper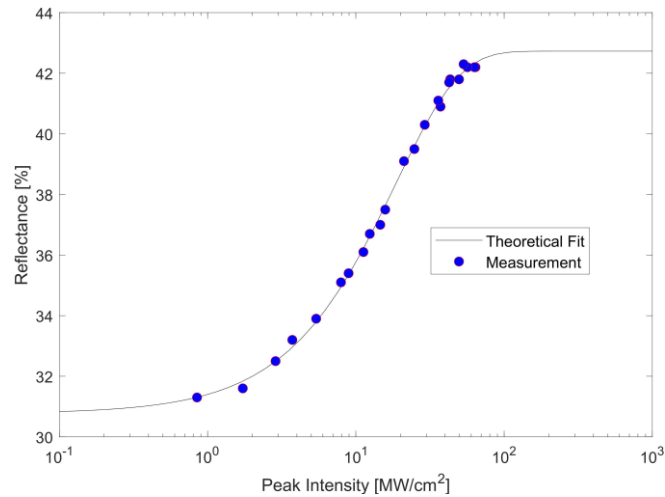ture of 0.24. The cavity is bounded by a fiber loop mirror (FLM) on one end and the MMI-SA on the other end. The FLM is constructed by joining the output ports of an 80:20 coupler and it provides 50% reflection at the lasing wavelength. A pump laser at a wavelength of 1550 nm is coupled to the TDF using a 1550/1900 wavelength division multiplexer (WDM). A second WDM is placed after TDF to remove any residual pump light. When the pump is switched on, the intensity dependent reflection of the MMI-SA results in formation of pulsed laser output at a wavelength of 1905 nm. An inline polarization controller is used to stabilize the laser oscillation. The laser output is observed using a photodetector with a bandwidth of 10 GHz that is connected to a real-time oscilloscope and an RF spectrum analyzer. The laser spectrum is monitored as well using an optical spectrum analyzer.
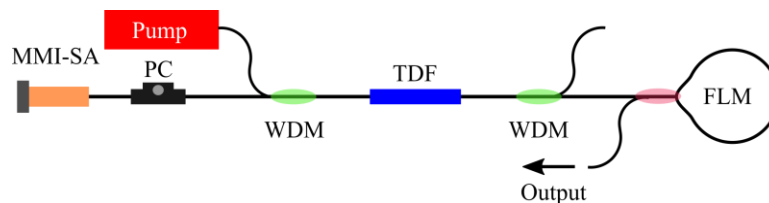
Figure 3.4. Laser cavity with fiber based MMI-SA. PC: Polarization controller, WDM: Wavelength division multiplexer, TDF: Thulium doped fiber, FLM: Fiber loop mirror.

3.3. Results and Discussion

After proper adjustment of polarization controller, modelock pulsed output is triggered in the laser cavity. Once the position of the polarization controller is fixed at the optimal state, the pulsation operation is self-starting. Figure 3.5 shows the pulsed laser output recorded using a real time oscilloscope with a bandwidth of 350 MHz. The pulse to pulse delay is 285 ns, which matches the cavity length of 29.7 m for single pulse per round trip.
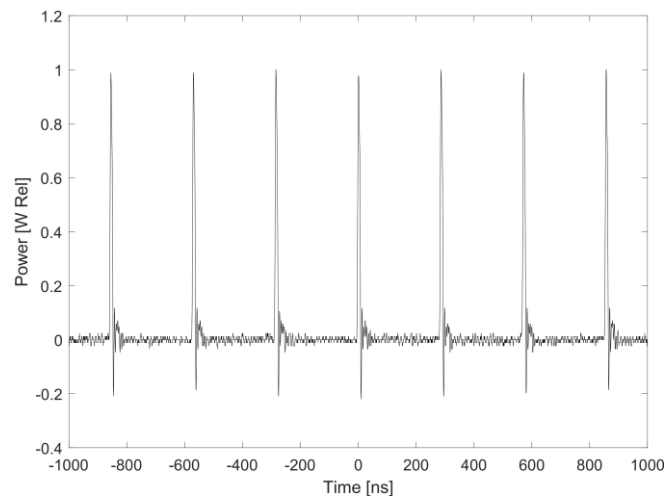
Figure 3.5. Pulse train at the fundamental repetition rate

Figure 3.6 shows the optical spectrum of the pulses recorded using an optical spectrum analyzer. The 3 dB bandwidth of the spectrum is 11.2 nm, which indicates a coherence time of ~345 fs. The absence of Kelly sidebands and relatively broad spectrum compared to soliton pulses at similar wavelength [8] is an indication of NLP formation, which is subsequently confirmed by an autocorrelation trace.
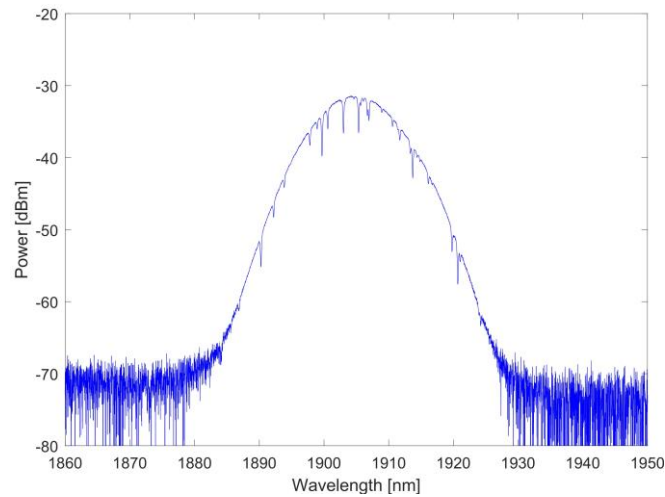
Figure 3.6. Optical spectrum of noise like pulses

Figure 3.7 shows the autocorrelation trance of the pulses recorded using a commercial autocorrelator. It shows a sharp coherent peak at zero delay on top of a broad pedestal limited by the temporal range of the autocorrelator. Such an autocorrelation trace is the signature of NLP [78,79]. The deconvolved FWHM of the coherent peak is ~365 fs, which represents the average duration of pulse features present in the NLP packet. Due to the high GVD (β_2 L= -3.97 ps^2) in the cavity, the cavity soliton breaks into a bunch of narrow pulses with random duration and peak intensity. These pulses are distributed randomly within the NLP packet [80]. The dispersion was decreased by shortening the roundtrip cavity length to 13 m. However, QS instabilities were dominant in the laser output in this configuration.
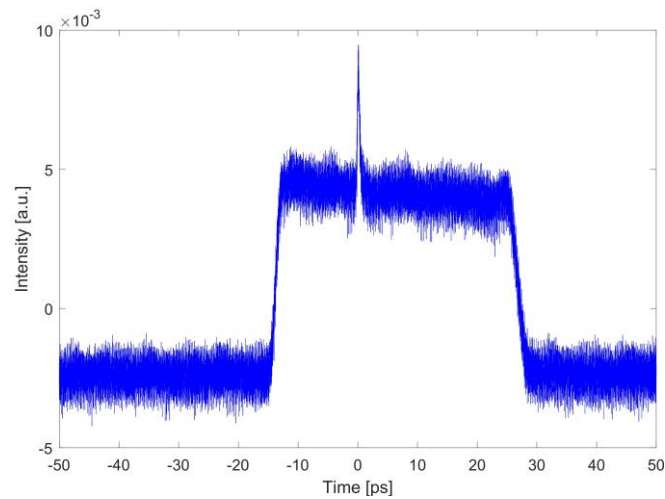
Figure 3.7. Autocorrelation trace showing narrow peak over a broad pedestal

Figure 3.8(a) shows the radio frequency (RF) spectrum of the modelocked laser output recorded with a resolution bandwidth of 1 kHz. The fundamental peak appears at 3.51 MHz, which matches with the pulse to pulse delay of 285 ns. A signal to noise ratio of 57 dB is observed from the measurement. The high signal to noise ratio and the absence of Q-switching sidebands indicate a stable pulse train. Figure 3.8(b) shows the RF spectrum over an extended range of 200 MHz. Peaks at integer multiples of fundamental repetition rate with a decreasing envelop are observed, which are a signature of stable continuous wave (CW)-mode locked laser.
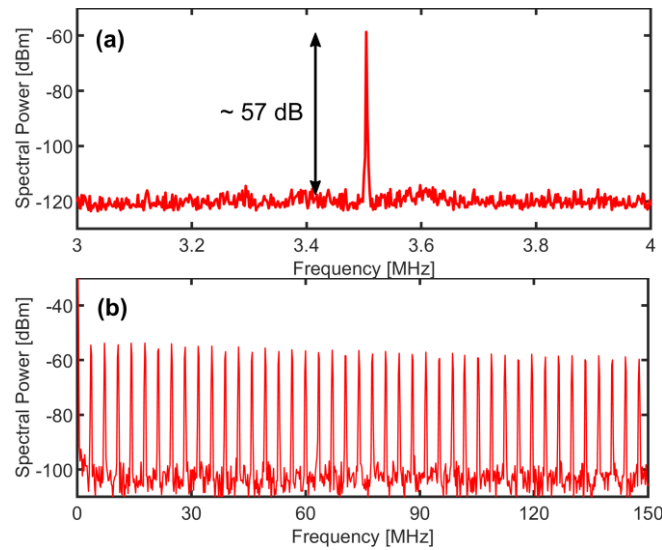
Figure 3.8. (a) Fundamental peak of RF spectrum of the TDFL. (b) RF spectrum over 200 MHz

frequency span

TDFL produces different outputs depending on the pump power as predicted by Ref. [81]. Figure 3.9 shows the average output power of the laser as function of the pump power. The laser has a threshold of 0.54 W and a slope efficiency of 1.02%. The maximum output power is 21.9 mW at pump power of 2.35 W. From the threshold to 0.7 W of pump power, the laser produces CW output without pulsation. Between 0.7 W and 1.3 W, the laser operates in QS-modelocking where a pulse train with varying envelop is produced. Beyond 1.3 W of pump power, laser operates in CW-ML state, where a pulse train with a constant envelop is generated. The next section provides a detailed QS- and CW- modelocked laser output.
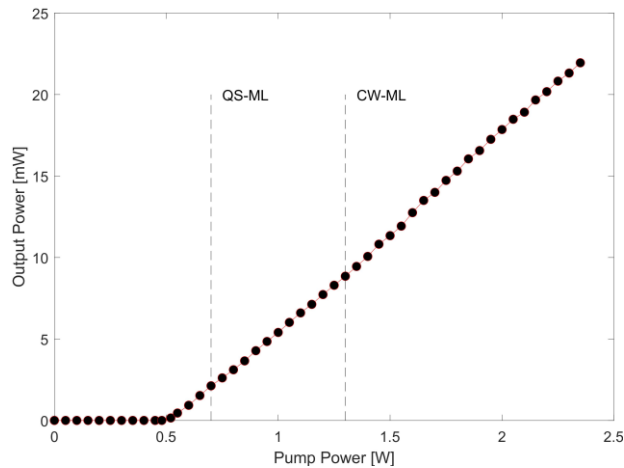
Figure 3.9. Average output power of the laser a function of pump power

3.4. CW- and QS- Modelocking

A laser cavity with saturable absorber (SA) can generate various kinds of pulsed outputs depending on the cavity parameters like gain, dispersion and nonlinearity, as well as parameters of the SA like saturation intensity and modulation depth. Continuous-wave modelocking (CWML) is the state where pulses with constant envelop are generated at cavity roundtrip rate (~10s of MHz) or its multiples. In Q-switched modelocking (QSML) regime, the pulses are modulated by a low frequency envelop of the order of ~10 kHz. This varying envelop is often referred to as Q-switching envelop. Depending on the pump power, the TDFL with GIMF based SA produced QSML and CWML output. This section presents an analysis of the laser output in these two regimes and highlights the key features that can be used to identify these states through oscilloscope trace, optical spectrum and RF-spectrum.

Laser output in time domain was recorded using a highspeed detector with a bandwidth 10 GHz and a real-time oscilloscope. Figure 3.10 shows the oscilloscope trace recorded for QSML

and CWML regime. For the CWML, pulse energy does not vary from pulse to pulse and envelop of the pulse train remains constant. Whereas, in QSML case, pulse energy seems to grow and decay with time, which leads to changing envelop with a frequency of ~87 kHz. It is important to note that the QSML output is quasi-stable and the frequency of the Q-switching envelop fluctuates due to thermal fluctuations in the cavity. In the CWML state, the pulse energy is higher than the saturation threshold of the gain medium and the laser is stable against QS-instabilities.
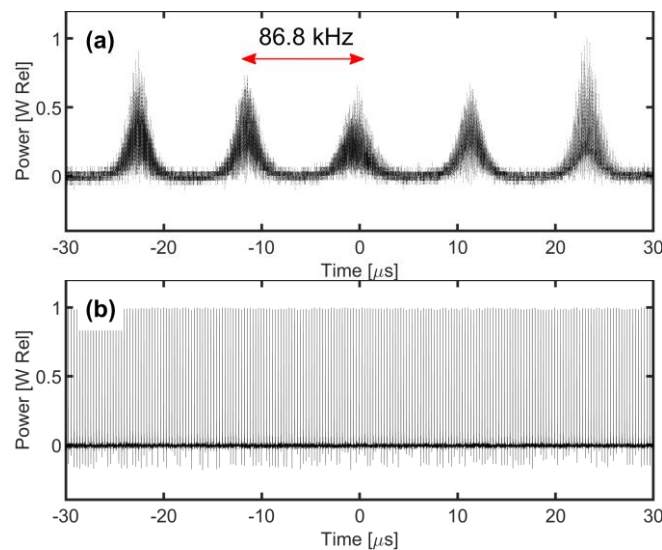
Figure 3.10. Lase output in (a) QS modelocked and (b) CW modelocked state.

Figure 3.11 shows a comparison of optical spectra of QSML and CWML outputs. The 3dB bandwidth for QSML and CWML output is 0.1 nm and 11.2 nm respectively. It is important to note that actual bandwidth for QSML is smaller than resolution of the optical spectrum analyzer. Furthermore, the optical spectrum for QSML laser is not different from single wavelength CW laser. By assuming a $\text{sech}^2(.)$ pulse shape, the 0.1 nm bandwidth indicates presence of pulses with duration > 42 ps. The CWML spectrum, on the other hand, shows presence of pulses of ~345 fs in the output.
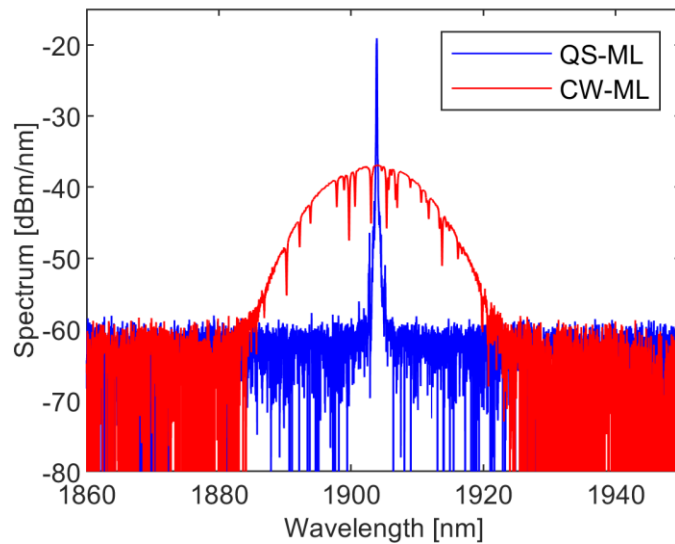
Figure 3.11. Optical spectrum of CWML and QSML laser

RF-spectrum is an excellent tool to analyze the stability of a modelocked laser. The RF-spectrum was recorded using electrical spectrum analyzer with a bandwidth of 2 GHz. Figure 3.12 shows the fundamental peaks in the RF-spectra of QSML and CWML outputs. The spectra are recorded using a resolution bandwidth of 1 kHz. Both spectra show a peak at the cavity repetition rate of 3.52 MHz. The QSML spectrum shows Q-switch side lobes at the pedestal of 3.52 MHz peak that arise due to the varying envelop in time domain. The signal to noise ratio in this case is only 31 dB. In contrast, the CWML spectrum shows a single peak with high signal to noise ratio of ~56 dB without any Q-switch side lobes. This spectrum indicates excellent pulse to pulse stability and it is consistent with the stable pulse train shown in Figure 3.10 (a).
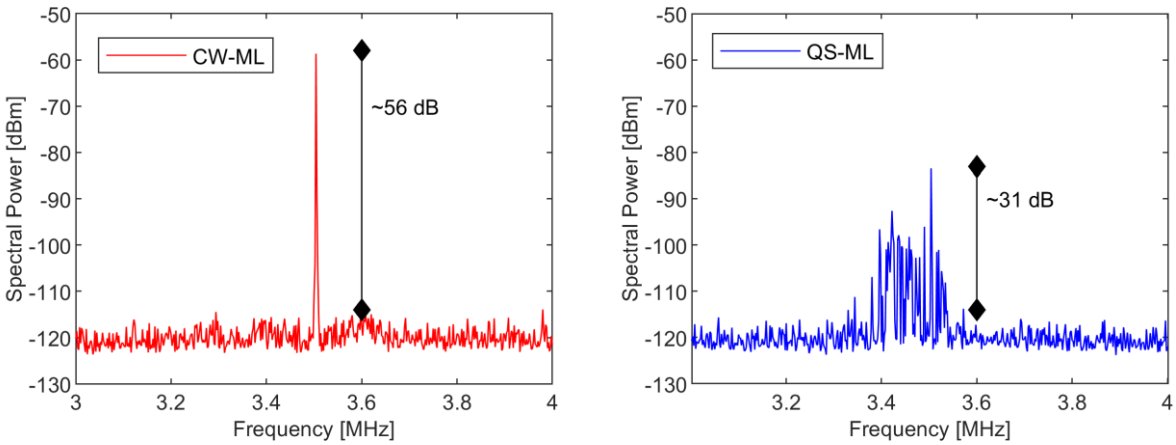
Figure 3.12. RF-spectrum of CWML and QSML laser at fundamental peak

Figure 3.13 shows the RF spectrum over a broader frequency span of 1 GHz. The resolution bandwidth for this measurement was 1 MHz. The CWML spectrum consist of peaks at multiple of cavity repetition rate (3.52 MHz) with a constantly decreasing envelop. Whereas, QSML spectrum is erratic and it only shows few of the peaks present CWML spectrum. It is also important to note that the QSML spectrum changed from one scan to the next because of the noisy nature of the QSML output, whereas the CWML was persistent over time.
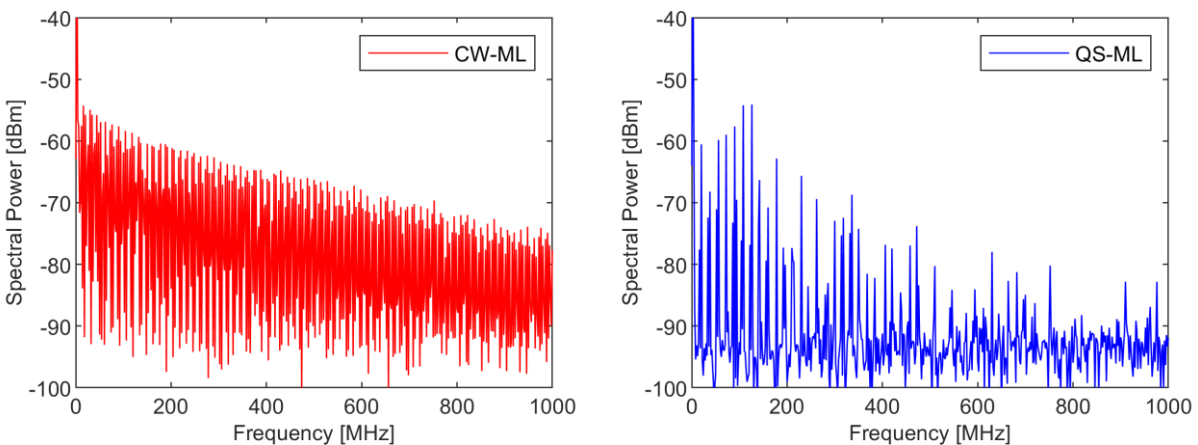
Figure 3.13. RF-Spectrum over frequency span of 1GHz

In conclusion, we have experimentally demonstrated the operation of a reflection mode MMI-SA based on silica graded index multimode fiber. The SA generates CW modelocked pulses in a linear laser cavity. The laser produces modelocked noise like pulses at a wavelength of 1905 nm. A detailed comparison of CW-modelocking and QS-modelocking is provided using experimental results. This simple cavity design will pave the way for creation of ultrafast pulsed lasers at longer wavelengths. Silica-based GIMF and SMF are used for the current experiment, but chalcogenide- or fluoride-based fibers could be used for the fabrication of a MMI-SA compatible with a mid-infrared fiber laser.

Chapter 4

Chalcogenide MMI Saturable Absorber

Chalcogenide glass (ChG) fibers are an attractive alternate to silica fibers due to their transmission window extending into the mid-IR wavelength range (2-12 µm) and their higher nonlinearity coefficient (n_2). In this chapter an MMI-SA based on As-S-Se MMF is presented. The SA structure consists of a 92 mm long As-S-Se step-index multimode fiber and provides a modulation depth of 14.7%. Using this structure in a linear cavity thulium doped fiber laser (TDFL), stable mode-locked operation and resembling pulse operation are demonstrated at a wavelength of 1.9 µm. This SA provides a simple all-fiber approach for the generation of optical pulses in the wavelength window of 2 µm and beyond.

MMI SAs consist of a multimode fiber sandwiched in between two single mode fibers, have been subject to intensive research efforts due to their all-fiber structure and ease of fabrication. While recent demonstrations of mode-locked lasers using MMI-SA [82–84] have focused on exploiting silica based MMF for modelocking lasers at 1 µm , 1.5 µm and 2 µm, MMI-

SAs that employs multimode fiber with high transmission above 2 μm wavelength are ideal for expanding MMI-SA modelocking to mid-infrared wavelength region.

In this experiment, an As-S-Se multimode fiber is used to form an MMI-SA. The MMF is transparent in the wavelength window of 1.2 μm to 4 μm and it can be configured for modelocking at any wavelength in this window. The functionality of the MMI-SA is demonstrated by insertion in a linear TDFL cavity, leading to a CW mode-locked regime. The proposed MMI-SA is described and characterized. Once the MMI-SA is inserted in a TDFL to trigger a pulsed regime, we observe two laser pulsation regimes that are a mode-locked regime and a resembling pulse regime at a wavelength of 1892 nm.

4.1. Processing of Chalcogenide Multimode Fiber

Chalcogenide glass (ChG) multimode fiber used in this experiment requires special processing. The fiber consists of an As-S-Se core and cladding with slightly different refractive indices. As the fiber is fragile, it also has a polymer coating to improve shock resistance during handling. First the fiber is pre-tapered using a custom-built setup that stretches the fiber while applying heat by an ironing heater at 195° C. This step removes any curvature present in the fiber and facilitates subsequent processing and light coupling. Afterwards, the fiber is cut roughly to the desired length and the polymer is removed from the tips to the fiber by dipping in dichloromethane for 60 seconds. Both ends of the fiber are then polished using the fiber polishing setup.

Figure 4.1 shows the fiber polishing setup. The fiber is polished using polishing pads 6 to 0 that gradually decrease the grain size. Pads 6 to 3 are used dry while, pads 2 to 0 require wetting

with isopropanol during polishing. A microscope camera is used monitor the contact of fiber tip with the polishing film. Figure 4.2 shows a microscope image of the facet after polishing along with the side profile of the fiber. The minimum fiber length achievable with this polishing setup is ~8 cm.
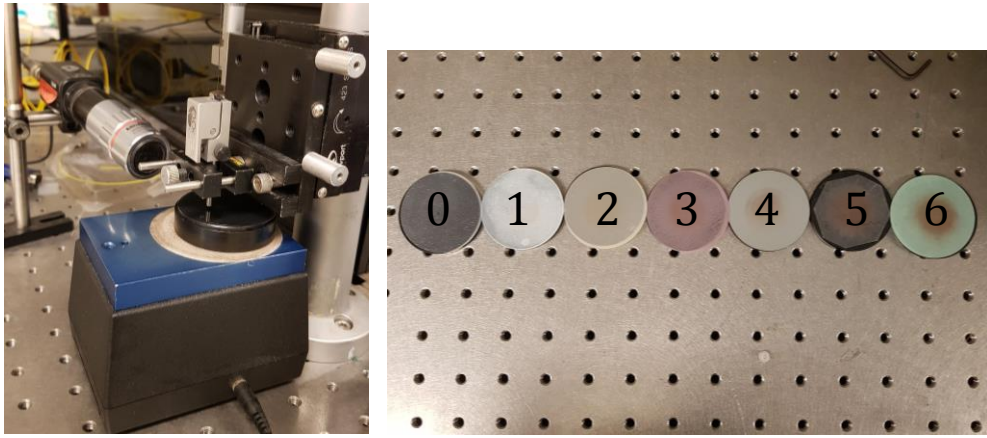

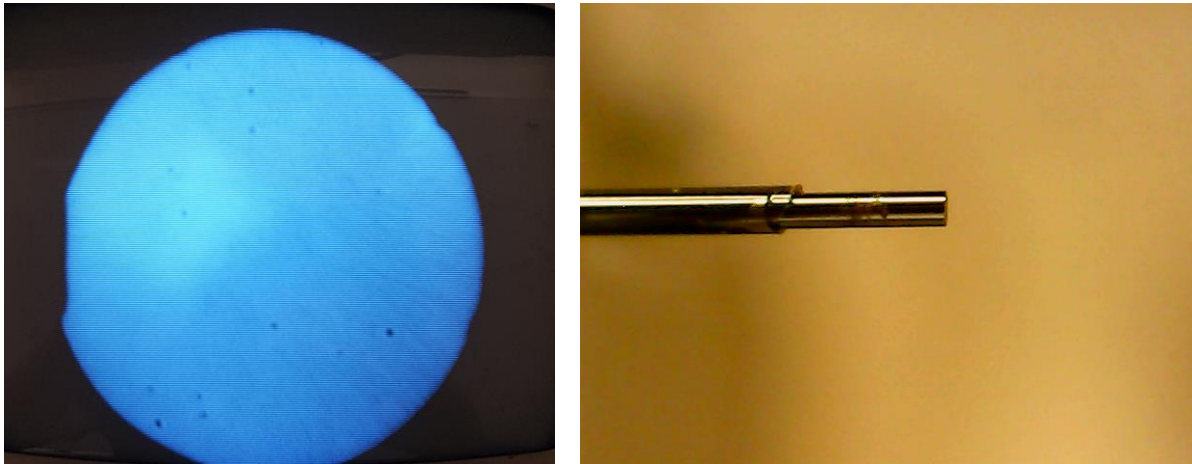
Figure 4.1 Fiber polishing setup and polishing pads

Figure 4.2. Microscope image of the polished fiber facet (left) and side profile of the fiber (right)

4.2. Chalcogenide MMF Saturable Absorber

Figure 4.3 shows a schematic of the proposed MMI-SA. It consists of a chalcogenide As-S-Se step index multimode fiber (MMF) with a length of 92 mm, core diameter of 16 μm, and numerical aperture of 0.28. The interest for the chalcogenide fiber is that it is three orders of magnitude more nonlinear than a silica-based MMF and thus a short length of this fiber is expected to trigger SA from less optical power than an equivalent silica-based MMF. A single mode fiber (SMF) is spliced to one end of the MMF using UV-epoxy. The same SMF serves as the input and output of the SA. A silica-based SMF is used for the current experiment, but a chalcogenide- or fluoride-based SMF could be used to preserve compatibility of the MMI-SA with the mid-infrared. A silver coated mirror is placed at the other end of the MMF to reflect light back to the MMF-SMF assembly.
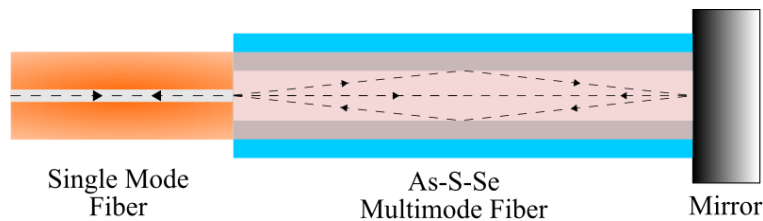
Figure 4.3. Nonlinear multimode interference saturable absorber.

Similar to the silica-based MMI-SA in chapter 3, the lateral offset between SMF and MMF is fixed such that it provides constructive interreference for high power input signal, leading to a power-dependent reflection coefficient. Hence the structure acts as a passive saturable absorber.

Figure 4.4 shows the mounting setup for the MMF. The MMF is held in place with two fiber stationary clamps while mirror and SMF are mounted on motion stages to provide tunable coupling. Two microscope cameras are used to monitor fiber alignment in vertical and horizontal

plane. Once the optimal alignment of input SMF is achieved, a UV epoxy is used to splice the SMF and MMF in place.
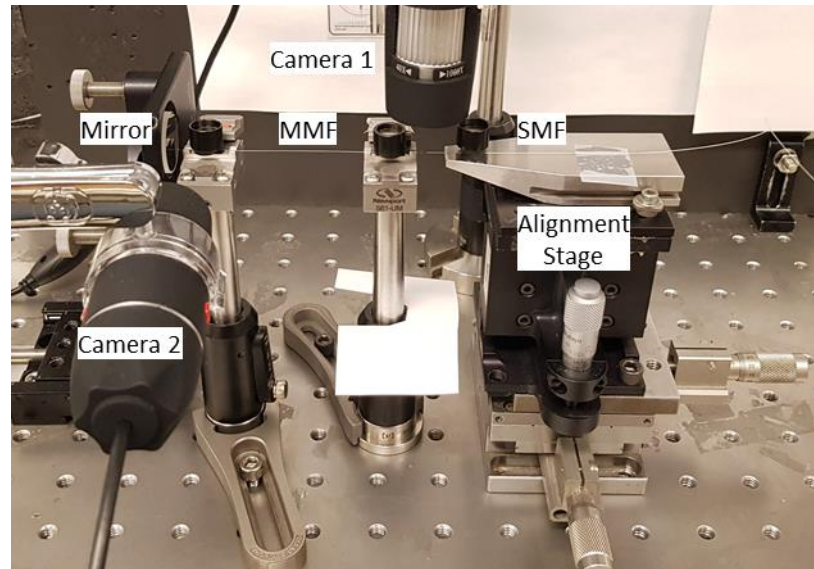
Figure 4.4 Mounting setup for MMI-SA with tunable MMF-SMF coupling

4.3. Saturation Measurement

Figure 4.5 shows the setup used to measure the nonlinear reflection coefficient of the MMI-SA. Pulses from a modelocked laser (MLL) with a central wavelength of 1937 nm and duration of 800 fs are sent to the MMI-SA through a circulator. A variable optical attenuator is used vary the power sent to the MMI-SA. The incident and reflected powers of the MMI-SA are recorded using calibrated power meters PM1 and PM2 respectively.
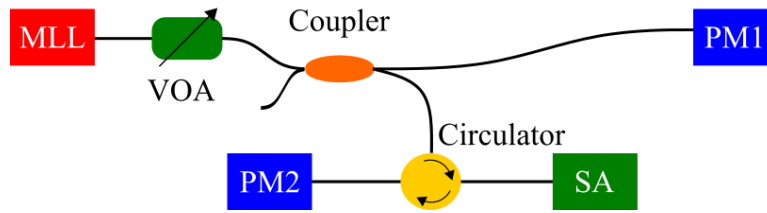
Figure 4.5. Characterization setup for MMI-SA. MLL: Mode-locked laser, VOA: Variable optical attenuator, PM: Power meter.

Figure 4.6 shows the reflection coefficient of the MMI-SA as a function of incident power. The theoretical reflection coefficient profile is given by

$$R = 1 - M \exp\left(-\frac{I}{I_{sat}}\right) - A_{ns}$$

Eq. 4.1

Here M is the modulation depth, A_{ns} is the non-saturable loss, and I_{sat} is the peak saturation intensity. From a fit with experimental data, their values are retrieved with $M = 14.7\%$, $A_{ns} = 82.5\%$, and $I_{sat} = 41.4$ kW/cm^2.
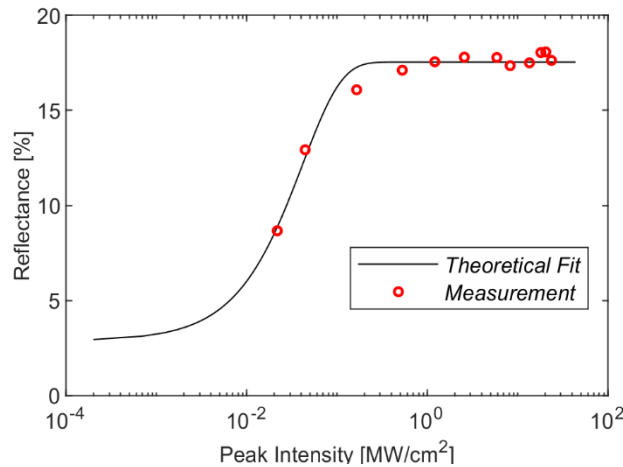
Figure 4.6. Reflectance of MMI-SA as a function of incident peak power.

4.4. Laser Cavity

Figure 4.7 shows a schematic of the proposed linear laser cavity triggered by the MMI-SA. The gain is provided by a 23 cm long thulium-doped fiber (TDF) with a core diameter of 6 μm and numerical aperture of 0.24. The cavity is bounded by a fiber loop mirror (FLM) on one end and the MMI-SA on the other end. The FLM is constructed by joining the output ports of an 80:20 coupler and provides 50% reflection at the lasing wavelength. A pump laser at a wavelength of 1550 nm is coupled to the TDF using a 1550/1900 wavelength division multiplexer (WDM). A second WDM is placed after the TDF to remove the residual pump light. A spool of SMF-28 with a length of 18.9 m is added to the cavity and the total cavity length is 30 m. Adding the additional SMF-28 increases the pulse to separation in laser output and facilitates observation of resembling pulse output. When the pump laser is on, the intensity dependent reflection of the MMI-SA results in the formation of pulses at a wavelength of 1892 nm. An inline polarization controller is used to stabilize the laser oscillation. The laser output is observed from one arm of the FLM using a photodetector with a bandwidth of 10 GHz connected to a real-time oscilloscope. The laser wavelength is recorded as well using an optical spectrum analyzer.
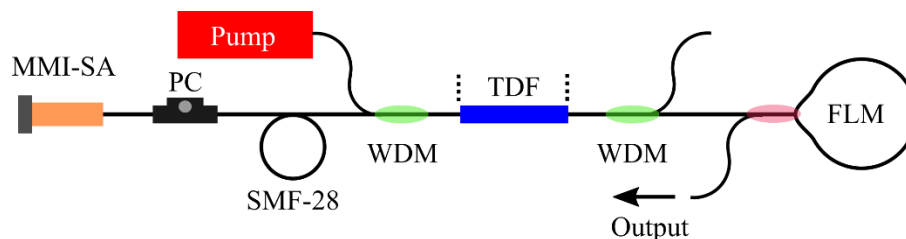
Figure 4.7. Laser cavity with fiber based MMI-SA. PC: Polarization controller,

WDM: Wavelength division multiplexer, TDF: Thulium doped fiber, FLM: Fiber loop mirror.

The dotted lines mark the sub-cavity Fabry Perot filter

4.5. Results and Discussion

Once the position of the polarization controller is properly adjusted, the pulsation operation is self-starting. Figure 4.8 shows an oscilloscope trace of the laser output. Instead of generating a single soliton modelocked pulse with repetition rate equal to cavity roundtrip time, the cavity generates resembling pulses. Resembling pulses are a group of identical pulses that are generated together with the repetition rate of the group being equal to cavity roundtrip time. The TDFL repetition rate is 3.46 MHz (or 1/289 ns), which matches the cavity length of 30 m. Presence of a sub-cavity in a linear laser cavity can give rise to formation of resembling pulses [85]. In the proposed TDFL cavity, partial reflections at SMF-TDF splice points create two sub-cavities. The reflection points are highlighted by dotted lines in Figure 4.7. The left sub-cavity consists of the MMI-SA, polarization controller, SMF-Spool, the left WDM and TDF, while the right sub-cavity consists of the TDF, right WDM and fiber loop mirror. These cavities have different roundtrip loss and in resonance condition, the right sub-cavity dominates the TDFL output. Length of this sub-cavity is 6.2 m and it matches the pulse to pulse delay of 59.2 ns in the laser output.
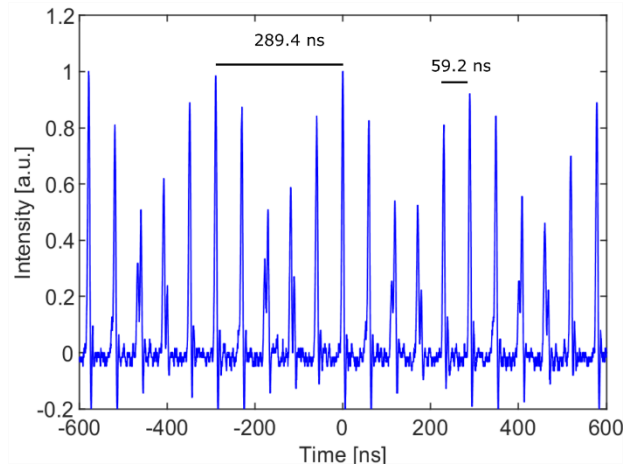
Figure 4.8. Resembling Pulse Output

Laser pulse train with a constant envelop can be generated if the parasitic reflection at SMF-TDF interface is suppressed by using angle polished connecters. Alternatively, when the length of the right sub-cavity is adjusted such that the total cavity length is an integer multiple of the sub-cavity length, the laser produces output pulse train with a constant envelop. Figure 4.9 shows the laser output when the sub-cavity length is reduced from 6.2 m to 5 m. Total cavity length is preserved at 30 m by adding 1.2 m of SMF outside the right sub-cavity. The oscilloscope trace shows a pulse to pulse delay in laser output is 48.4 ns, which is consistent with the 5 m sub-cavity. In this case, the pulses from subsequent reflections better overlap with one another and create a pulsed laser output of quasi-constant envelop. The subsequent results are for this cavity configuration.
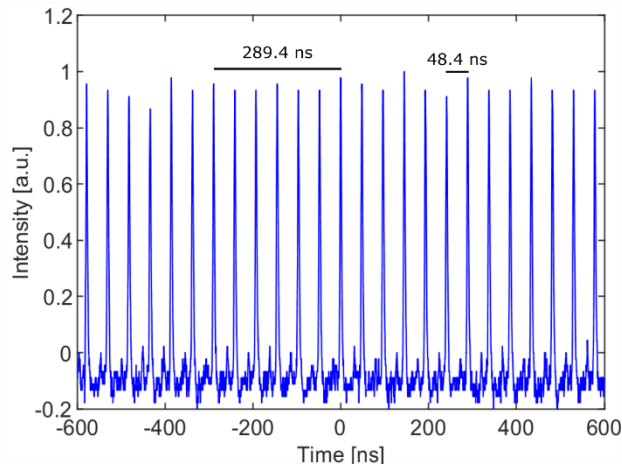
Figure 4.9. Laser output showing constant envelop pulse train

Figure 4.10 shows a single isolated pulse in the time domain. The full width half maximum (FWHM) duration is 3.4 ns, which is five orders of magnitude broader than the pulses achieved with silica based MMI-SA. Figure 4.10 shows the optical spectrum of the laser output. The spectrum shows a single peak centered at a wavelength of 1892 nm. The peak width is spectrally limited by the resolution bandwidth of the optical spectrum analyzer, which is set at 0.1 nm for this measurement. The refractive index mismatch at As-S-Se to SMF interface leads to parasitic reflections in the laser cavity. These reflections limit the broadening of laser spectrum through Fabry Perot filtering. This narrow spectrum results in formation of broad nano-second pulses as observed in Figure 4.10. Using a multimode fiber with a refractive index similar to the SMF would not limit the spectral broadening and it would lead to generation of narrow femtosecond pulses as demonstrated in chapter 3. Hence it is recommended to fabricate the MMI-SA using a ZBLAN multimode fiber when working with ZBLAN laser cavities in the mid-IR. Alternatively, using a ChG MMF and with ChG SMF for MMI-SA can also limit parasitic

reflections. Lastly, suppressing the parasitic reflections by angled polishing the SMF can also mitigate the limiting of spectral broadening.
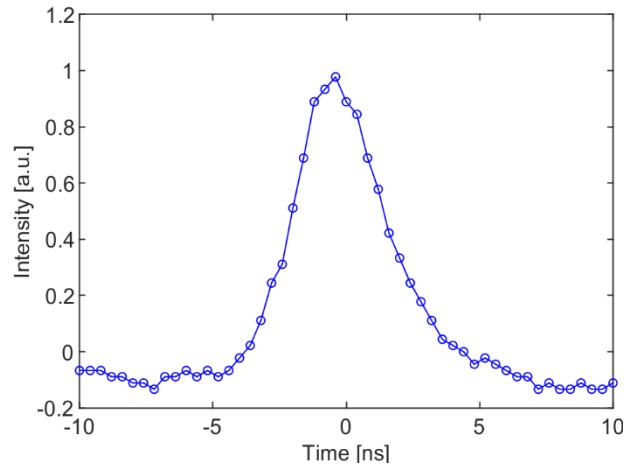
Figure 4.10. Single isolated pulse in the time domain showing FWHM of 3.4 ns.
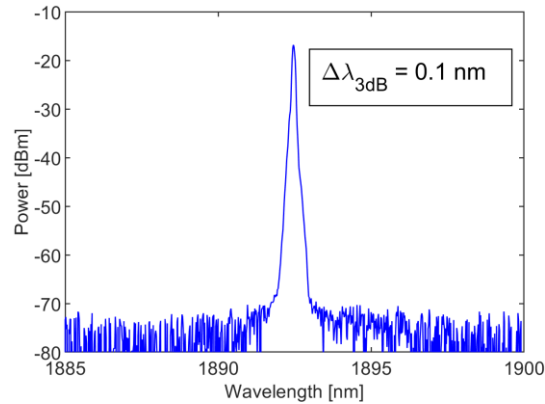
Figure 4.11 Optical spectrum of laser output showing a single peak at 1892 nm.

Figure 4.12 shows the light-current (L-I) curve of this laser that is the average output power of the laser as function of the pump current/power. The laser has a threshold of 0.33 W and a slope efficiency of 2.0%, without any sign of saturation. The maximum output power is 15.2 mW at pump power of 1.1 W. The vertical axis on the right-hand side of Figure 4.12 shows the pulse peak power calculated using a pulse duration of 3.4 ns and a repetition rate of 20.7 MHz. The maximum

peak power is 216 mW. Maximum average power and peak power are limited by the maximum available pump power.
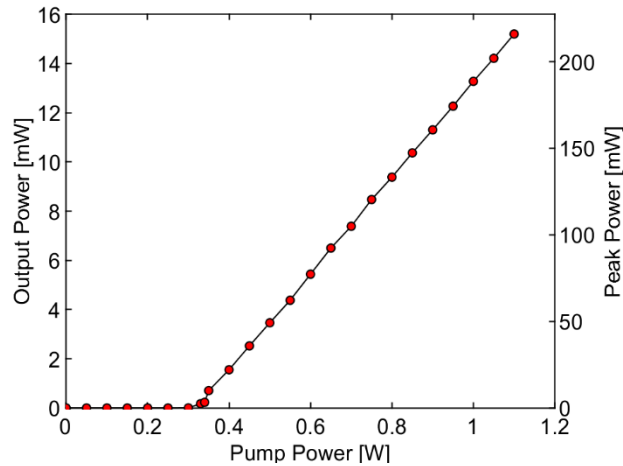
Figure 4.12. Laser output power and pulse peak power as a function of pump power.

In summary, we have experimentally demonstrated the generation of laser pulses using nonlinear multimode interference in a step-index multimode As-S-Se fiber used in a reflection mode. We have investigated and mitigated generation of resembling pulses due to sub-cavity reflections in the laser. In future, the reflection mode design of the MMI-SA can be utilized for fabrication of modelocked linear cavity lasers at mid-IR wavelengths beyond 2 μm.

Conclusion and Future Work

A fiber based saturable absorber that can operate beyond 2 µm wavelength is vital for development of economical, robust and compact modelocked fiber lasers in the mid-IR wavelength region. This thesis studied the design and performance of a multimode fiber based SA that operates in reflection mode. The reflection mode design also makes this SA compatible with linear cavity laser configuration. Linear cavity lasers can be modelocked without the need of optical components like optical isolators and circulators, which makes them more cost-effective.

First, the operation of a MMI-SA based on silica graded index multimode fiber has been experimentally demonstrated. The SA generates CW modelocked pulses in a linear laser cavity with thulium doped fiber as a gain medium. The laser produces noise like pulses with pulse width of 365 fs at a wavelength of 1905 nm. Afterwards, the silica MMF is replaced with a mid-IR compatible As-S-Se MMF. Using the second SA, stable mode-locked operation and resembling pulse operation are demonstrated at a wavelength of 1892 nm.

This work uncovers important design considerations for modelocked mid-IR fiber laser. The saturable absorber demonstrated in this work is easy to fabricate and it enables modelocking without the need of an optical isolator. Furthermore, it can be adopted in the future to achieve modelocking over a broad wavelength window including mid-IR. Optical nonlinearity and

dispersion in the laser cavity can be optimized further to enhance the modelocked laser output.

Other applications of the MMI device like refractive index sensing can also be explored.

References

1. A. Schliesser, N. Picqué, and T. W. Hänsch, "Mid-infrared frequency combs," Nat. Photonics **6**, 440–449 (2012).

2. P. Tang, Z. Qin, J. Liu, C. Zhao, G. Xie, S. Wen, and L. Qian, "Watt-level passively mode-locked Er^3+-doped ZBLAN fiber laser at 2.8 μm," Opt. Lett. **40**, 4855 (2015).

3. X. H. Zhang, J. L. Adam, and B. Bureau, "Chalcogenide Glasses," Springer Handbooks **2019**, 525–552 (2019).

4. I. Cozmuta, S. Cozic, M. Poulain, S. Poulain, and J. R. Martini, "Breaking the silica ceiling: ZBLAN-based opportunities for photonics applications," in *Optical Components and Materials XVII*, M. J. Digonnet and S. Jiang, eds. (SPIE, 2020), p. 25.

5. T. Chen, Q. Zhang, Y. Zhang, X. Li, H. Zhang, and W. Xia, "All-fiber passively mode-locked laser using nonlinear multimode interference of step-index multimode fiber," Photonics Res. **6**, 1033 (2018).

6. S. Dai, Y. Wang, X. Peng, P. Zhang, X. Wang, and Y. Xu, "A review of mid-infrared supercontinuum generation in chalcogenide glass fibers," Appl. Sci. **8**, (2018).

7. E. Nazemosadat and A. Mafi, "Nonlinear multimodal interference and saturable absorption using a short graded-index multimode optical fiber," J. Opt. Soc. Am. B **30**, 1357 (2013).

8. H. Li, Z. Wang, C. Li, J. Zhang, and S. Xu, "Mode-locked Tm fiber laser using SMF-SIMF-GIMF-SMF fiber structure as a saturable absorber," Opt. Express **25**, 26546 (2017).

9. Z. Wang, D. N. Wang, F. Yang, L. Li, C. Zhao, B. Xu, S. Jin, S. Cao, and Z. Fang, "Er-

Doped Mode-Locked Fiber Laser with a Hybrid Structure of a Step-Index-Graded-Index Multimode Fiber as the Saturable Absorber," J. Light. Technol. **35**, 5280–5285 (2017).

10.   U. Teğin and B. Ortaç, "All-fiber all-normal-dispersion femtosecond laser with nonlinear multimodal interference-based saturable absorber," Opt. InfoBase Conf. Pap. **Part F140**-, 1611–1614 (2019).

11.   C. Wu, Y. Yao, Q. Wu, Y. Yang, Z. Wu, Y. Yang, J. Tian, and K. Xu, "Different types of noise-like pulse in a nonlinear multimodal interference based mode-locked fiber laser," Opt. Laser Technol. **147**, 107681 (2022).

12.   F. Zhao, Y. Wang, H. Wang, Z. Yan, X. Hu, W. Zhang, T. Zhang, and K. Zhou, "Ultrafast soliton and stretched-pulse switchable mode-locked fiber laser with hybrid structure of multimode fiber based saturable absorber," Sci. Rep. **8**, 1–7 (2018).

13.   K. Zhang and M. Rochette, "All-Fiber Saturable Absorber Using Nonlinear Multimode Interference in a Chalcogenide Fiber," J. Light. Technol. **38**, 6321–6326 (2020).

14.   Z. Lv, Z. Yang, D. D. Song, F. Li, Y. Yang, X. Yang, Y. Wang, Q. Li, and W. Zhao, "Observation of dissipative soliton bound states in a nonlinear multimodal interference based all-fiber all-normal-dispersion mode-locking laser," Opt. Laser Technol. **119**, 105626 (2019).

15.   C. Baker and M. Rochette, "Highly nonlinear hybrid AsSe-AsSe-PMMA microtapers," Opt. Express **18**, 12391 (2010).

16.   L. Li, N. Abdukerim, and M. Rochette, "Chalcogenide optical microwires cladded with fluorine-based CYTOP," Opt. Express **24**, 18931–18937 (2016).

17.   L. Li, A. Al-Kadry, N. Abdukerim, and M. Rochette, "Design, fabrication and characterization of PC, COP and PMMA-cladded As2 Se3 microwires," Opt. Mater. Express **6**, 912–921 (2016).

18.   C. Baker and M. Rochette, "High nonlinearity and single-mode transmission in tapered multimode As2Se3-PMMA fibers," IEEE Photonics J. **4**, 960–969 (2012).

19. M. Rochette, "The tapering of optical fibers," in *Mid-Infrared Fibre Photonics: Glass Materials, Fibre Fabrication and Processing, Laser Sources and Devices*, S. Jakson, R. Vallee, and M. Bernier, eds. (Elsevier, 2021).

20. M. Rezaei and M. Rochette, "All-chalcogenide single-mode optical fiber couplers," Opt. Lett. **44**, 5266–5269 (2019).

21. F. Tavakoli, A. Rekik, and M. Rochette, "Broadband and wavelength-dependent chalcogenide optical fiber couplers," IEEE Photonics Technol. Lett. **29**, 735–738 (2017).

22. K. Zhang, I. Alamgir, and M. Rochette, "Midinfrared compatible tunable bandpass filter based on multimode interference in chalcogenide fiber," J. Light. Technol. **38**, 857–863 (2020).

23. K. Zhang, Y.-A. Peter, and M. Rochette, "Chalcogenide Fabry–Perot fiber tunable filter," IEEE Photonics Technol. Lett. **30**, 2013–2016 (2018).

24. R. Ahmad and M. Rochette, "Photosensitivity at 1550 nm and Bragg grating inscription in As2Se3 chalcogenide microwires," Appl. Phys. Lett. **99**, 61109 (2011).

25. R. Ahmad, M. Rochette, and C. Baker, "Fabrication of Bragg gratings in subwavelength diameter As 2 Se 3 chalcogenide wires," Opt. Lett. **36**, 2886–2888 (2011).

26. F. Vanier, F. Côté, M. El Amraoui, Y. Messaddeq, Y.-A. Peter, and M. Rochette, "Low-threshold lasing at 1975 nm in thulium-doped tellurite glass microspheres," Opt. Lett. **40**, 5227–5230 (2015).

27. F. Vanier, Y.-A. Peter, and M. Rochette, "Cascaded Raman lasing in packaged high quality As2S3 microspheres," Opt. Express **22**, 28731–28739 (2014).

28. F. Vanier, M. Rochette, N. Godbout, and Y.-A. Peter, "Raman lasing in As2S3 high-Q whispering gallery mode resonators," Opt. Lett. **38**, 4966–4969 (2013).

29. M. I. Kayes and M. Rochette, "Fourier transform spectroscopy by repetition rate sweeping of a single electro-optic frequency comb," Opt. Lett. **43**, 967–970 (2018).

30.　N. Abdukerim, I. Alamgir, and M. Rochette, "Pulse characterization by cross-phase modulation in chalcogenide glass," Opt. Lett. **43**, 4771–4774 (2018).

31.　N. Abdukerim, I. Alamgir, and M. Rochette, "All-fiber frequency-resolved optical gating pulse characterization from chalcogenide glass," Opt. Lett. **43**, 3228–3231 (2018).

32.　I. Alamgir, M. H. M. Shamim, W. Correr, Y. Messaddeq, and M. Rochette, "Mid-infrared soliton self-frequency shift in chalcogenide glass," Opt. Lett. **46**, 5513–5516 (2021).

33.　R. Kormokar, M. H. M. Shamim, and M. Rochette, "High-order analytical formulation of soliton self-frequency shift," JOSA B **38**, 466–475 (2021).

34.　I. Alamgir, F. St-Hilaire, and M. Rochette, "All-fiber nonlinear optical wavelength conversion system from the C-band to the mid-infrared," Opt. Lett. **45**, 857–860 (2020).

35.　I. Alamgir, N. Abdukerim, and M. Rochette, "In situ fabrication of far-detuned optical fiber wavelength converters," Opt. Lett. **44**, 4467–4470 (2019).

36.　M. Rochette, "Design and fabrication of nonlinear optical waveguides for far-detuned wavelength conversion to the mid-infrared," Adv. Opt. Technol. **7**, 321–326 (2018).

37.　L. Li, N. Abdukerim, and M. Rochette, "Mid-infrared wavelength conversion from As 2 Se 3 microwires," Opt. Lett. **42**, 639–642 (2017).

38.　M. R. Fernández-Ruiz, L. Lei, M. Rochette, and J. Azaña, "All-optical wavelength conversion based on time-domain holography," Opt. Express **23**, 22847–22856 (2015).

39.　T. Godin, Y. Combes, R. Ahmad, M. Rochette, T. Sylvestre, and J. M. Dudley, "Far-detuned mid-infrared frequency conversion via normal dispersion modulation instability in chalcogenide microwires," Opt. Lett. **39**, 1885–1888 (2014).

40.　A. Al-Kadry and M. Rochette, "Maximized soliton self-frequency shift in non-uniform microwires by the control of third-order dispersion perturbation," J. Light. Technol. **31**, 1462–1467 (2013).

41.　A. M. Al-kadry and M. Rochette, "Mid-infrared sources based on the soliton self-frequency

shift," JOSA B **29**, 1347–1355 (2012).

42. S. Venck, F. St-Hilaire, L. Brilland, A. N. Ghosh, R. Chahal, C. Caillaud, M. Meneghetti, J. Troles, F. Joulain, and S. Cozic, "2–10 µm Mid-Infrared Fiber-Based Supercontinuum Laser Source: Experiment and Simulation," Laser Photon. Rev. **14**, 2000011 (2020).

43. D. D. Hudson, S. Antipov, L. Li, I. Alamgir, T. Hu, M. El Amraoui, Y. Messaddeq, M. Rochette, S. D. Jackson, and A. Fuerbach, "Toward all-fiber supercontinuum spanning the mid-infrared," Optica **4**, 1163–1166 (2017).

44. A. Al-Kadry, L. Li, M. El Amraoui, T. North, Y. Messaddeq, and M. Rochette, "Broadband supercontinuum generation in all-normal dispersion chalcogenide microwires," Opt. Lett. **40**, 4687–4690 (2015).

45. A. Al-Kadry, M. El Amraoui, Y. Messaddeq, and M. Rochette, "Two octaves mid-infrared supercontinuum generation in As2Se3 microwires," Opt. Express **22**, 31131–31137 (2014).

46. A. Al-kadry, C. Baker, M. El Amraoui, Y. Messaddeq, and M. Rochette, "Broadband supercontinuum generation in As2Se3 chalcogenide wires by avoiding the two-photon absorption effects," Opt. Lett. **38**, 1185–1187 (2013).

47. W. Lin, M. Desjardins-Carrière, B. Sévigny, J. Magné, and M. Rochette, "Raman suppression within the gain fiber of high-power fiber lasers," Appl. Opt. **59**, 9660–9666 (2020).

48. M. I. Kayes and M. Rochette, "Precise distance measurement by a single electro-optic frequency comb," IEEE Photonics Technol. Lett. **31**, 775–778 (2019).

49. M. I. Kayes, N. Abdukerim, A. Rekik, and M. Rochette, "Free-running mode-locked laser based dual-comb spectroscopy," Opt. Lett. **43**, 5809–5812 (2018).

50. M. I. Kayes and M. Rochette, "Optical frequency comb generation with ultra-narrow spectral lines," Opt. Lett. **42**, 2718–2721 (2017).

51. N. Abdukerim, L. Li, M. El Amraoui, Y. Messaddeq, and M. Rochette, "2 µm Raman fiber

laser based on a multimaterial chalcogenide microwire," Appl. Phys. Lett. **110**, 161103 (2017).

52.   N. Abdukerim, L. Li, and M. Rochette, "Chalcogenide-based optical parametric oscillator at 2 μm," Opt. Lett. **41**, 4364–4367 (2016).

53.   R. Ahmad and M. Rochette, "Chalcogenide optical parametric oscillator," Opt. Express **20**, 10095–10099 (2012).

54.   R. Ahmad and M. Rochette, "High efficiency and ultra broadband optical parametric four-wave mixing in chalcogenide-PMMA hybrid microwires," Opt. Express **20**, 9572–9580 (2012).

55.   A. Al-Kadry, M. El Amraoui, Y. Messaddeq, and M. Rochette, "Mode-locked fiber laser based on chalcogenide microwires," Opt. Lett. **40**, 4309–4312 (2015).

56.   E. Meyer-Scott, A. Dot, R. Ahmad, L. Li, M. Rochette, and T. Jennewein, "Power-efficient production of photon pairs in a tapered chalcogenide microwire," Appl. Phys. Lett. **106**, 81111 (2015).

57.   A. Dot, E. Meyer-Scott, R. Ahmad, M. Rochette, and T. Jennewein, "Converting one photon into two via four-wave mixing in optical fibers," Phys. Rev. A **90**, 43808 (2014).

58.   R. Ahmad and M. Rochette, "All-chalcogenide Raman-parametric laser, wavelength converter, and amplifier in a single microwire," IEEE J. Sel. Top. Quantum Electron. **20**, 299–304 (2014).

59.   A. Salehiomran, R. Modirnia, B. Boulet, and M. Rochette, "Optical parametric oscillator longitudinal modes suppression based on Smith predictor control scheme," Ieee Trans. Control Syst. Technol. **22**, 2064–2072 (2013).

60.   A. Salehiomran and M. Rochette, "A nonlinear model for the operation of fiber optical parametric oscillators in the steady state," IEEE Photonics Technol. Lett. **25**, 981–984 (2013).

61.   R. Ahmad and M. Rochette, "Raman lasing in a chalcogenide microwire-based Fabry–Perot cavity," Opt. Lett. **37**, 4549–4551 (2012).

62.   R. Ahmad and M. Rochette, "Chalcogenide microwire based Raman laser," Appl. Phys. Lett. **101**, 101110 (2012).

63.   N. Abdukerim, M. I. Kayes, A. Rekik, and M. Rochette, "Bidirectional mode-locked thulium-doped fiber laser," Appl. Opt. **57**, 7198–7202 (2018).

64.   T. North, A. Al-Kadry, and M. Rochette, "Analysis of self-pulsating sources based on cascaded regeneration and soliton self-frequency shifting," IEEE J. Sel. Top. Quantum Electron. **20**, 612–618 (2014).

65.   T. North and M. Rochette, "Regenerative self-pulsating sources of large bandwidths," Opt. Lett. **39**, 174–177 (2014).

66.   T. North and M. Rochette, "Analysis of self-pulsating sources based on regenerative SPM: ignition, pulse characteristics and stability," J. Light. Technol. **31**, 3700–3706 (2013).

67.   T. North and M. Rochette, "Raman-induced noiselike pulses in a highly nonlinear and dispersive all-fiber ring laser," Opt. Lett. **38**, 890–892 (2013).

68.   T. North and M. Rochette, "Broadband self-pulsating fiber laser based on soliton self-frequency shift and regenerative self-phase modulation," Opt. Lett. **37**, 2799–2801 (2012).

69.   T. North and M. Rochette, "Fabrication and characterization of a pulsed fiber ring laser based on As 2 S 3," Opt. Lett. **37**, 716–718 (2012).

70.   K. Sun, M. Rochette, and L. R. Chen, "Output characterization of a self-pulsating and aperiodic optical fiber source based on cascaded regeneration," Opt. Express **17**, 10419–10432 (2009).

71.   M. Rochette, L. R. Chen, K. Sun, and J. Hernandez-Cordero, "Multiwavelength and tunable self-pulsating fiber cavity based on regenerative SPM spectral broadening and filtering," IEEE Photonics Technol. Lett. **20**, 1497–1499 (2008).

72.   C. Jia, B. J. Shastri, N. Abdukerim, M. Rochette, P. R. Prucnal, M. Saad, and L. R. Chen, "Passively synchronized Q-switched and mode-locked dual-band Tm3+: ZBLAN fiber lasers using a common graphene saturable absorber," Sci. Rep. **6**, 1–9 (2016).

73.   M. Ma, M. Rochette, and L. R. Chen, "Generating chirped microwave pulses using an integrated distributed Fabry–Pérot cavity in silicon-on-insulator," IEEE Photonics J. **7**, 1–6 (2015).

74.   J. Wang, R. Ashrafi, M. Rochette, and L. R. Chen, "Chirped microwave pulse generation using an integrated SiP Bragg grating in a Sagnac loop," IEEE Photonics Technol. Lett. **27**, 1876–1879 (2015).

75.   U. Keller, "Materials and new approaches for ultrashort pulse lasers," Curr. Opin. Solid State Mater. Sci. **1**, 218–224 (1996).

76.   J. Kim and Y. Song, "Ultralow-noise mode-locked fiber lasers and frequency combs: principles, status, and applications," Adv. Opt. Photonics **8**, 465 (2016).

77.   G. Agrawal, *Applications of Nonlinear Fiber Optics, 2nd Edition* (2008).

78.   T. North and M. Rochette, "Raman-induced noiselike pulses in a highly nonlinear and dispersive all-fiber ring laser," Opt. Lett. **38**, 890 (2013).

79.   M. Horowitz, Y. Barad, and Y. Silberberg, "Noiselike pulses with a broadband spectrum generated from an erbium-doped fiber laser [TN 3]," Opt. Lett. **22**, 799 (1997).

80.   J. C. Hernandez-Garcia, O. Pottiez, J. M. Estudillo-Ayala, and R. Rojas-Laguna, "Numerical analysis of a broadband spectrum generated in a standard fiber by noise-like pulses from a passively mode-locked fiber laser," Opt. Commun. **285**, 1915–1919 (2012).

81.   C. Hönninger, R. Paschotta, F. Morier-Genoud, M. Moser, and U. Keller, "Q-switching stability limits of continuous-wave passive mode locking," J. Opt. Soc. Am. B **16**, 46 (1999).

82.   H. Zhang, Y. Lyu, C. Wei, H. Shi, Q. Li, S. Jiang, and Y. Liu, "Watt-level fibre MOPA in

2.9 μ m water vapor window seeded by Q-switched fibre laser," Laser Phys. Lett. **15**, 095106 (2018).

83.　Z. Wang, D. N. Wang, F. Yang, L. Li, C.-L. Zhao, B. Xu, S. Jin, S.-Y. Cao, and Z.-J. Fang, "Stretched graded-index multimode optical fiber as a saturable absorber for erbium-doped fiber laser mode locking," Opt. Lett. **43**, 2078 (2018).

84.　H. Jiang, H. Li, F. Hu, X. Ren, C. Li, and S. Xu, "Mode-locked Tm Fiber Laser with a tapered GIMF SA based on Nonlinear Multimode Interference effect," IEEE Photonics Technol. Lett. **32**, 1–1 (2020).

85.　W. Chen, W. Lin, T. Qiao, and Z. Yang, "Additive mode-locked resembling pulses in a Tm-doped fiber laser with a hybrid cavity configuration," Opt. Express **23**, 28012 (2015).